Direct Sun-Driven Artificial Heliotropism for Solar Energy Harvesting Based on a Photo-Thermomechanical Liquid-Crystal Elastomer Nanocomposite

*Chensha Li, Ye Liu, Xuezhen Huang, and Hongrui Jiang**

Inspired by heliotropism in nature, artificial heliotropic devices that can follow the sun for increased light interception are realized. The mechanism of the artificial heliotropism is realized via direct actuation by the sunlight, eliminating the need for additional mechatronic components and resultant energy consumption. For this purpose, a novel reversible photo-thermomechanical liquid crystalline elastomer (LCE) nanocomposite is developed that can be directly driven by natural sunlight and possesses strong actuation capability. Using the LCE nanocomposite actuators, the artificial heliotropic devices show full-range heliotropism in both laboratory and in-field tests. As a result, significant increase in the photocurrent output from the solar cells in the artificial heliotropic devices is observed.

1. Introduction

Heliotropism is an intriguing attribute of some plants whose leaves or flowers, when directlydriven by the sunlight, can follow the sun for increased light interception.[1] Inspired by nature, we have realized artificial heliotropic devices, utilizing actuators based on a photo-thermomechanical liquid crystalline elastomer (LCE) nanocomposite that we have developed. The mechanism of our artificial heliotropism is realized via direct actuation by the sunlight, eliminating the need for additional mechatronic components and resultant energy consumption. Our LCE nanocomposite can be directly driven by natural sunlight, has reversible photomechanical response, and possesses strong actuation capability. Using these LCE nanocomposite actuators, our artificial heliotropic devices showed full-range heliotropism in both laboratory and in-field tests. As a result, significant increase in the photocurrent output from the solar cells in our artificial heliotropic devices was observed, depending on the incident light direction.

C. S. Li, Y. Liu, X. Huang, Prof. H. Jiang
Department of Electrical and Computer Engineering
University of Wisconsin-Madison
1415 Engineering Drive, Madison, WI, 53706, USA
E-mail: hongrui@engr.wisc.edu
Prof. H. Jiang
Materials Science Program
University of Wisconsin-Madison
1415 Engineering Drive, Madison, WI, 53706, USA

DOI: 10.1002/adfm.201202038

Figure 1 shows the concept of our artificial heliotropism. The solar cells are installed on a platform that is connected to actuators and elastically supported so that it can tilt under the actuation force (Figure 1a). At any time instant, actuator(s) facing the incoming sunlight would be in a contracted state, while other actuators not exposed to the sunlight would be in the relaxed state. Consequently, the platform holding the solar cells would be driven by the contracted actuator(s), and self-adaptively tilt towards the sunlight, hence the artificial heliotropism and increased photocurrent output from the solar cells (Figure 1b). Note that the actuation/tilting and the resultant artificial heliotropism are directly driven by the sunlight. Different from the current man-made solar tracking systems which are generally realized through mechatronic designs,[2,3] our approach possesses the elegance and simplicity in natural heliotropism, and avoids the use of complicated electro-mechanical actuator and feedback systems, and their inherent high cost and power consumption, which unfortunately significantly negates the gain offered by power generation. Compared to other passive solar tracking systems,[3] such as those based on thermal expansion of gases or metals, our approach realizes full-range tracking with a much less complicated system. Our approach is also self-contained, thus being able to be combined with other methods to increase the solar cell output, including enhancing the conversion efficiency[4–12] and implementing concentrators.[13–16]

Light-driven materials promise important roles in many applications, as light is a clean energy source and can be remotely and conveniently manipulated.[17] It is highly desired to develop materials that can convert the energy of natural sunlight into mechanical work. Our artificial heliotropism concept requires actuators that can directly respond to the natural sunlight with mechanical actuation, and such response must also be reversible. There is yet a material that can fulfill all these requirements. Our solution is to develop actuators based on photo-thermomechanical liquid crystal elastomer (LCE) materials. LCEs are unique materials with properties of both liquid crystals and elastomers; the self-organization nature of liquid crystal systems and the flexibility from the rubber elasticity allow for large and reversible anisotropic dimensional change in response to applied stimuli.[18–23] They are therefore

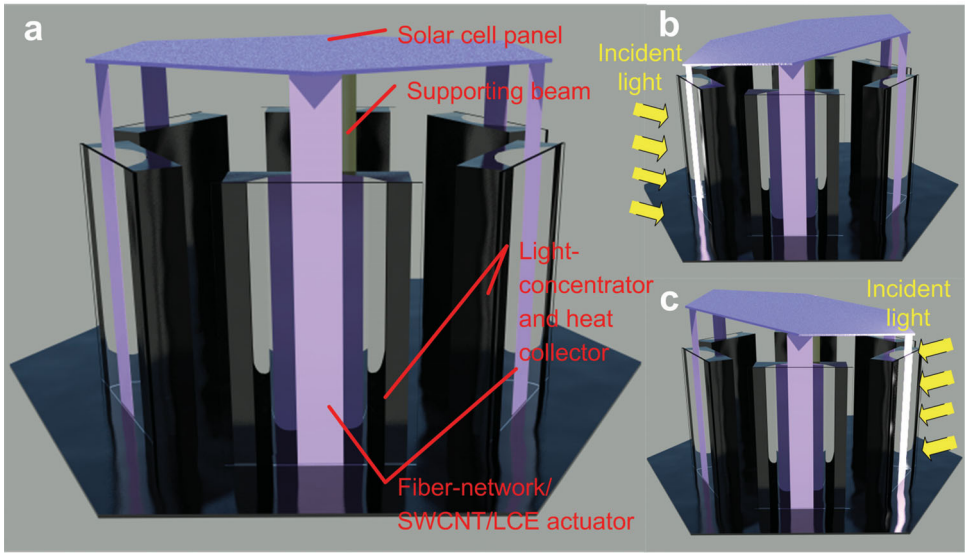

Figure 1. Concept of the artificial heliotropism. a) 3D schematic of the system. b,c) 3D schematic of the heliotropic behavior. The actuator(s) facing the sun contracts, tilting the solar cell towards the sunlight.

promising for applications in smart actuators, artificial muscles and microelectromechanical systems (MEMS).[24–31]

2. Results and Discussion

2.1. Photo-Thermomechanical LCE Nanocomposite

In order to realize sunlight driven actuators for the artificial heliotropism in our work, we developed a LCE nanocomposite formed by incorporating single-wall carbon nanotubes (SWCNTs) into a matrix of nematic LCE. SWCNTs can efficiently absorb and convert photon energy into thermal energy and have excellent thermal conductivities,[32] thus acting as nanoscale heat source and thermal conduction pathway to effectively heat the LCE matrix, elevating its temperature to above the nematic–isotropic transition temperature (T_{ni}), changing the nematic order, and leading to a reversible axial contraction and mechanical actuation.[33] This photo-thermomechanical LCE nanocomposite is capable of utilizing the photon energy of the wide spectrum of light simultaneously to realize photo-thermomechanical actuation. Therefore, different from those photomechanical responsive LCE materials based on incorporating photoisomerizable molecules or molecular chromophores into the LCE network, whose photo actuation can only be induced by filtered light to specific wavelengths,[23,24,26–31,34,35] our LCE nanocomposite can fully utilize the energy from light sources for mechanical actuation. Moreover, the incorporation of SWCNTs into this LCE matrix also significantly decreases the T_{ni} of the material,[33] thus lowering the threshold for its photo-thermomechanical actuation. These two factors hence enable the actuation of the LCE nanocomposite by natural sunlight.

Furthermore, in order to enhance the actuation capability of the LCE nanocomposites for implementation in artificial heliotropism, we successfully incorporated polyurethane fiber-networks as the reinforcement phase into the nematic LCE matrix. The fabrication of the polyurethane fiber-network/SWCNT/LCE composite, which was performed through a two-stage crosslinking coupled with a drawing process, is shown in **Figure 2** and detailed in the Experimental Section. The anisotropic alignment of the mesogens in LCE matrix of the polyurethane fiber-network/SWCNT/LCE composite was investigated by using X-ray scattering. **Figure 3**a exhibits a characteristic X-ray diffraction pattern of an aligned nematic liquid crystal[19] with a pronounced azimuthal distribution of intensity at $2\theta = 20.15°$, corresponding to a dimension of lateral packing mesogenic units ≈0.48 nm. The introduction of polyurethane fiber-network in nematic LCE matrix brings about a broad ring in the X-ray diffraction pattern, which can be identified by comparing with the X-ray diffraction pattern of the bare polyurethane fiber-network shown in Figure S1 (Supporting Information). However, the uniaxially ordered LCE matrix creates two areas of high intensity on the ring, which is confirmed by the two peaks in the azimuthal integration of wide-angle diffraction arc, as shown in Figure 3b. Some smectic fluctuations can bring weak small angle reflections on the equator in the X-ray diffraction pattern,[19] which results in the weak shoulder peaks between two large peaks in Figure 3b. The result proves an LCE nematic-phase texture with the mesogenic units being well uniaxially aligned. The SWCNTs incorporated into the LCE did not have a specific orientation.[33] The DSC measurement of phase transitions indicates that the nematic-isotropic transition temperature (T_{ni}) of the fiber-network/SWCNT/LCE also significantly lowered compared to that of the blank nematic LCE. As shown in Figure 3c, the T_{ni} of the blank nematic LCE itself is 80.3 °C, while the T_{ni} of the fiber-network/SWCNT/LCE nanocomposite is about 68 °C. This much lowered T_{ni} (<70 °C) significantly facilitates the actuation of the fiber-network/SWCNT/LCE by the natural sunlight. The fiber-network/SWCNT/LCE nanocomposite

Adv. Funct. Mater. **2012**,
DOI: 10.1002/adfm.201202038

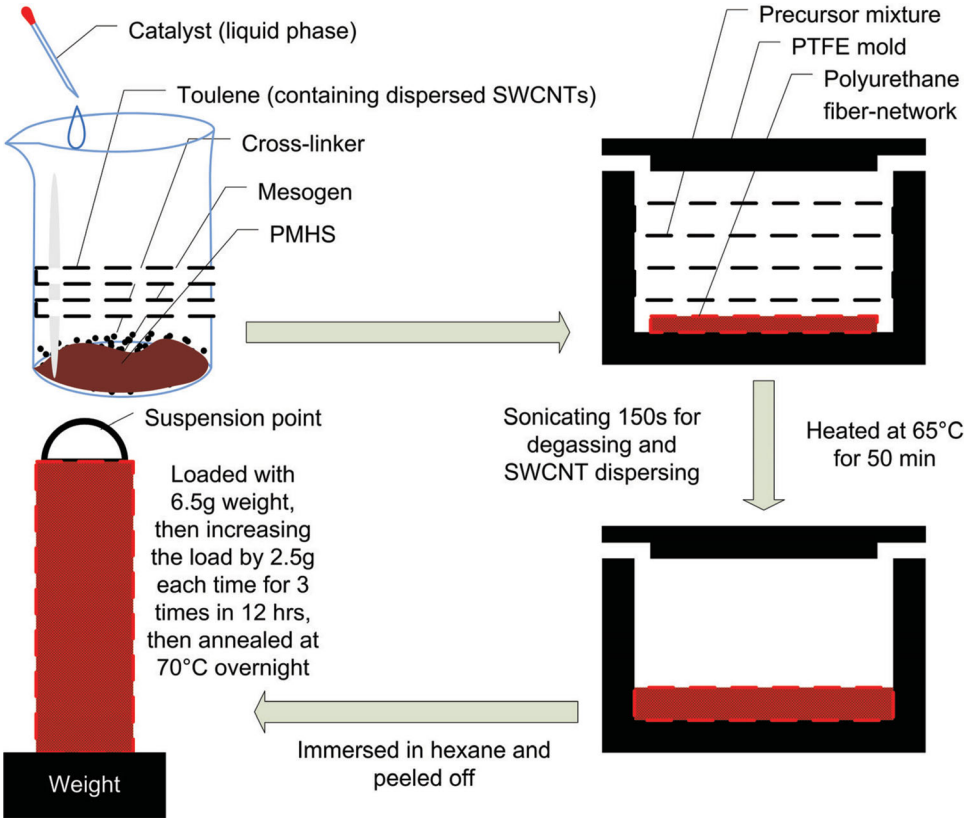

Figure 2. Fabrication process for the fiber-network/SWCNT/LCE nanocomposite films.

demonstrated strong photo-thermomechanical response characteristic. Figure 3d–f shows the photo-thermomechanical response of a fiber-network/SWCNT/LCE nanocomposite film under a white light radiation (intensity: 230 mW cm^{-2}) at room temperature of 25 °C. The fiber-network/SWCNT/LCE nanocomposite film exhibits a rapid and uniform contraction of 27% in several seconds. After the light source was removed, the film restored to it original length in several seconds.

Incorporating SWCNT/LCE with polyurethane fiber-network greatly enhanced the mechanical properties of the actuator material, especially the mechanical strength at high temperature. In our experiments, we found that the SWCNT/LCE composites alone as the actuator for artificial heliotropism without the reinforcement of polyurethane fiber network was prone to fracture, during the photo-thermomechanical actuation process under a high temperature above their T_{ni} and a large loading for a long time. So far, there has been no report on using continuous fibers as the reinforcement phases for nematic LCE matrices. It has been reported that filling carbon nanotubes into the LCE matrices can improve their mechanical performances.[33,34,36] In principle, the mechanical performances of composites could be much enhanced with the reinforcement of continuous fibers.[37] We used a continuous fiber network, a polyurethane fiber network, as the reinforcement phase of the LCE composites. The fiber-network/SWCNT/LCE composites could easily serve as actuators without apparent damage and degradation for hundreds of cycles. The rupture strength of the fiber-network/SWCNT/LCE film at a temperature higher than its T_{ni} (i.e., in isotropic phase and contracted state) was measured to be around 800 kPa, while that of the SWCNT/LCE without the fiber-network reinforcement under the same condition was about 160 kPa. The fiber-network/SWCNT/LCE thus possesses sufficient actuation capability for the artificial heliotropic devices due to its much improved mechanical property compared to the SWCNT/LCE nanocomposite.

2.2. Light Concentrator and Heat Collector (LCHC)

In order for the effective actuation of the LCE nanocomposite actuators under natural sunlight, we have also designed a relatively simple structure to accompany them. This structure (**Figure 4**a) serves as both a light concentrator and a heat collector (LCHC). The high-reflectivity multilayer polymer film at the inner back of the structure forms a cylindrical mirror, and the actuator is placed close to its focal line. The distribution of the intensity of the reflected light at the plane where the actuator is placed is simulated using Zemax. As shown in Figure 4b, the major portion of the incident light is collected by the cylindrical mirror and focused back onto the actuator plane. The position of the focal line translates as the direction of the incident light varies. As shown in Figure 4c,d, when the altitude and the azimuth of the incident light both deviate around 30° from the normal incidence, the focused line moves vertically by 5.3 mm and laterally by 5.3 mm. Thus, in our design, we use actuators with widths of more than 12 mm and lengths

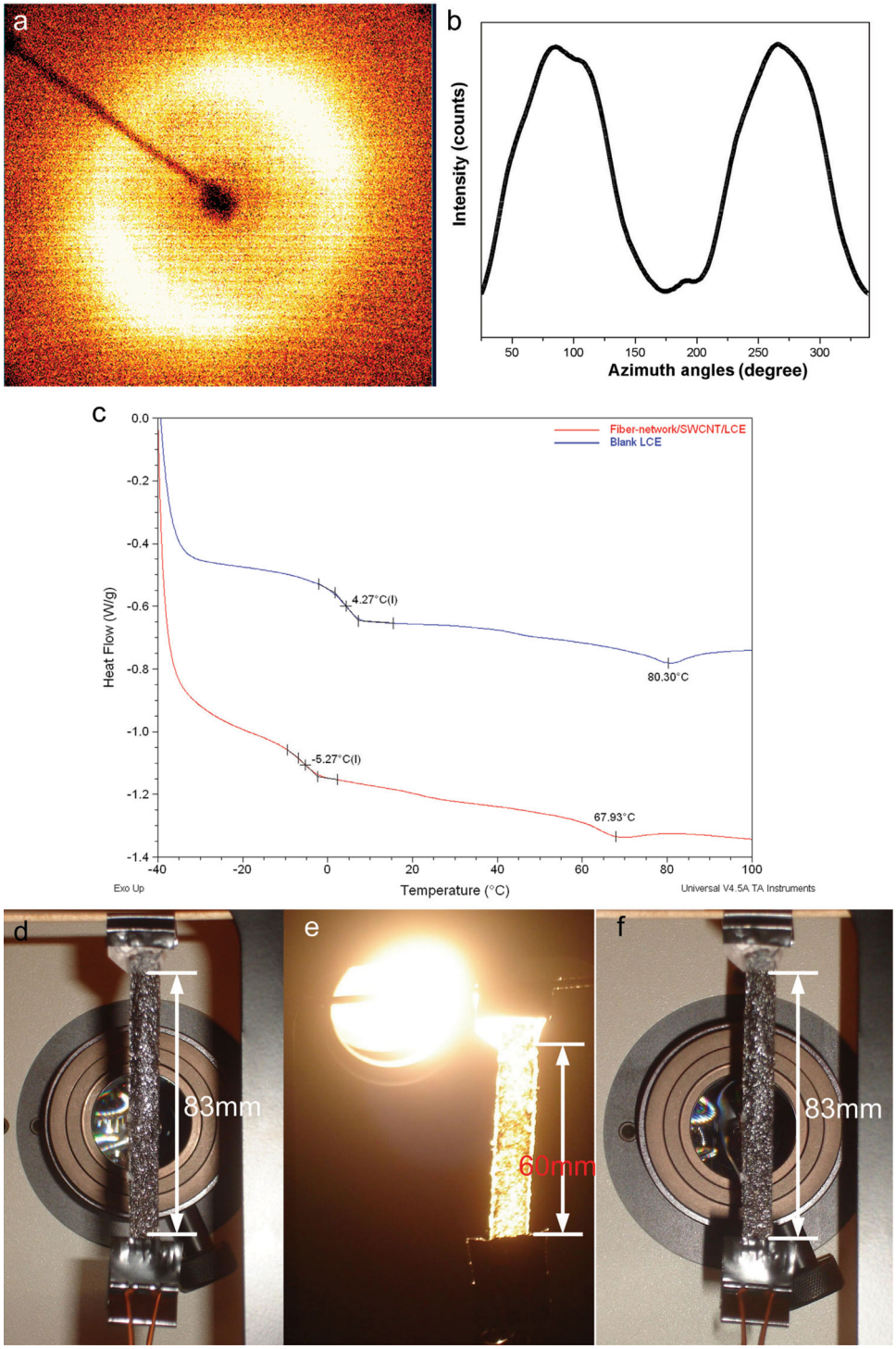

Figure 3. a) An X-ray diffraction pattern obtained from a fiber-network/SWCNT/LCE sample. b) Azimuthal intensity distribution of the X-ray diffraction pattern of fiber-network/SWCNT/LCE. c) DSC data curves of the blank LCE and fiber-network/SWCNT/LCE nanocomposite. d,e,f) Optical images of the photoactuation of a fiber-network/SWCNT/LCE film. The film, with dimensions of 83 mm × 12 mm × 0.8 mm and a load of 3 g weight, is irradiated by an incident white light of 230 mW cm^{-2}. d) The initial state of the fiber-network/SWCNT/LCE film. e) It contracts to a stable length of 60 mm, which is about 73% of the initial length, after 12 s under irradiation. f) It recovers to its initial length 12 s after the light source is switched off.

of more than 75 mm to ensure that the major portion of the focused light would be onto the actuator film. The black polytetrafluoroethylene (PTFE) bulk of the LCHC structure helps maintain a higher local temperature around the actuator by reducing the heat conduction with its low thermal conductivity (≈0.25 W m^{-1} K^{-1}). The LCHC chamber is also semi-sealed by

Adv. Funct. Mater. **2012**,
DOI: 10.1002/adfm.201202038

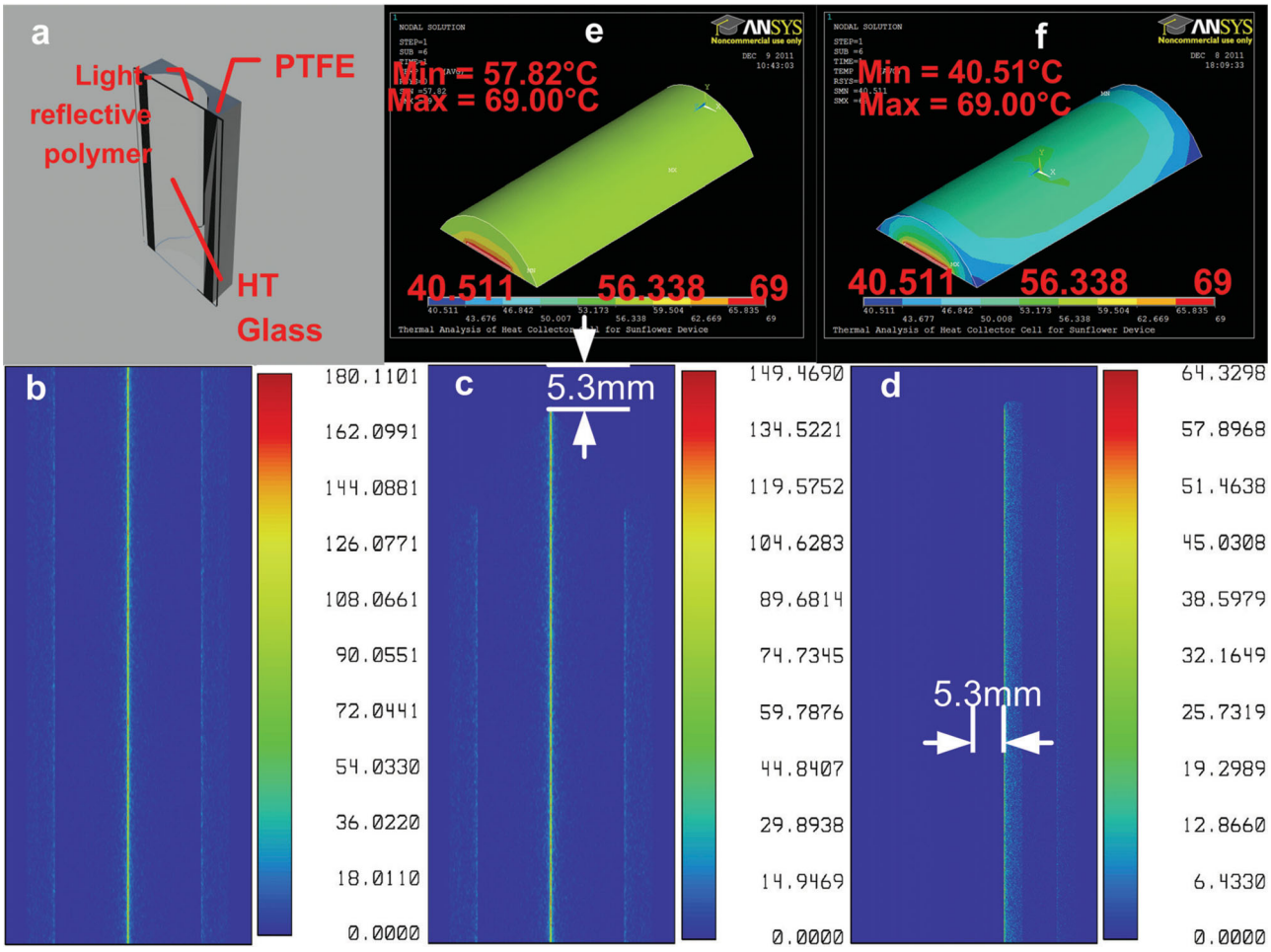

Figure 4. a) 3D schematic of the LCHC and its components. b) Zemax simulation of the intensity distribution of the collected and refocused light from a normal incident (0° altitude, 180° azimuth) collimated light beam (intensity: 100 mW cm^{-2}), on the plane where the actuator resides. c) Intensity distribution on the same plane with an incident collimated light illuminating from 30° altitude and 180° azimuth. d) Intensity distribution at the same plane with an incident collimated light illuminating from 30° altitude and 150° azimuth. e) Contour plot of the air temperature distribution inside the LCHC by simulation using ANSYS, considering the radiation absorption of the black PTFE bulk. f) Contour plot of the air temperature distribution around the actuator without an LCHC. The temperature of the actuator was set at 69 °C ($>T_{ni}$) and the ambient temperature was set at 22 °C. Comparing (g) and (h), the heat dissipation with LCHC is much less than without an LCHC.

a high-transmittance glass slide, greatly reducing the airflow and heat convection around the actuator. Simulation result by ANSYS shows that the LCHC is able to maintain the temperature of the air inside the LCHC (Figure 4e), while without the LCHC the heat dissipates to the ambient much more easily (Figure 4f). As a result, it is easier for the temperature of the fiber-network/SWCNT/LCE actuator to stay above its T_{ni} and maintain its contracted state when the actuator is facing the sunlight. More detail on the LCHC structure and the simulation parameters is given in the Supporting Information (Figure S2–S8).

2.3. Artificial Heliotropism Performance

We then characterized the heliotropic capability of a single unit consisting of one LCHC and one fiber-network/SWCNT/LCE film actuator (≈80 mm × 12 mm × 0.8 mm) placed at the focal line of the cylindrical mirror of the LCHC. In-field tests were performed between July and August 2011 in Madison, WI, USA. Two units were utilized but only one would face towards the sun in these tests. **Figure 5**a,b shows the result during one in-field test at 43 ° 4′20″N, 89 ° 24 ′ 44″W on August 3, 2011. Initially the device was blocked from the sunlight. Then the actuator in the right unit was made facing the sun and started to contract. In ≈110 s, it stopped contraction and the solar cell was tilted towards the sun by 16.3°. More results of these in-field tests are included in the Supporting Information (Movies 1–3). The increase in the photocurrent output from the solar cells due to artificial heliotropism vs. the direction of the incident light was characterized in our laboratory so that the tests would be less affected by natural elements such as wind, haze, and clouds. In these laboratory tests, the solar cells were initially horizontal (the photocurrent output at this initial state was the baseline), and the incident light was from a white light source (intensity: 100 mW cm^{-2}; partially

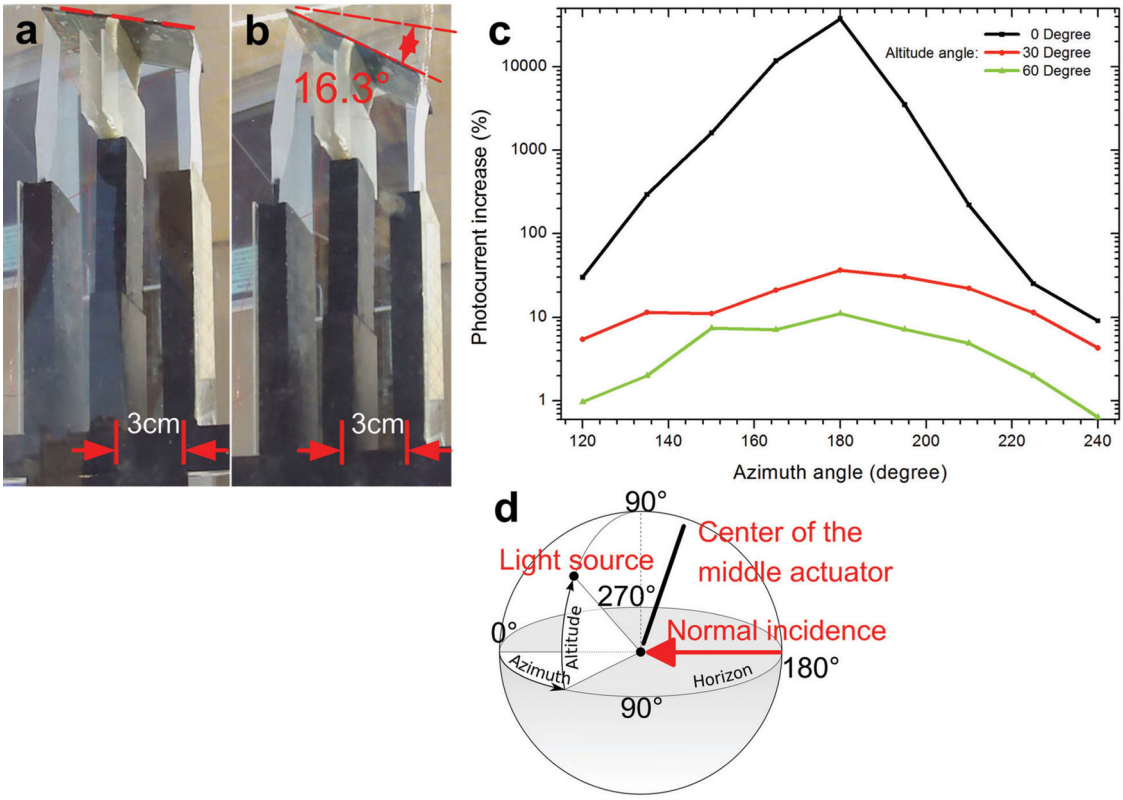

Figure 5. Heliotropic behavior of a 2-LCHC-actuator-unit device during one in-field testing (a,b) and resultant photocurrent increase with a single LCHC-actuator unit (c). The in-field test was conducted at 43° 4′20″N, 89° 24′ 44″W on August 3, 2011. Initially the device was blocked from the sunlight. a) The actuator was just exposed to the sunlight and began to contract. b) After 110 s, the actuator achieved a full contraction state and the solar cell was tilted by 16.3°. c) Photocurrent increase owing to artificial heliotropism with a single LCHC-actuator unit. The incident light was kept at 100 mW cm^{-2} but was from different directions. d) The altitude-azimuth coordinate system used. The origin was the center of the actuator facing the light. The normal incidence direction was 0° altitude, 180° azimuth.

collimated; spot diameter: 101.6 mm). Figure 5c shows the results. The direction of the incident light is identified by the altitude angle and the azimuth angle of the light source with respect to the center of the actuator, considering the direction of "normal incidence" to the actuator as 0° altitude and 180° azimuth (Figure 5d) shows the altitude-azimuth coordinate system used; more detail is included in the Supporting Information). Heliotropism owing to one LCHC-actuator unit resulted in large increase in the photocurrent output at normal incidence, and by more than 100% in the 150°-210° azimuth range at 0° altitude (note that the base photocurrent was low in these situations). When the altitude angle of the light source increased to 60°, increase in the photocurrent was still more than 4%. Altitude more than 60° (e.g., 70°) left little room for increasing the photocurrent by heliotropism, as it was already fairly close to normal radiation onto the solar cells. From Figure 5, an empirical estimation of the effective heliotropic range for one LCHC-actuator unit is thus 0° to +60° in altitude angle and between ±30° in azimuth angle, with respect to the normal incidence.

Considering the information of the heliotropic range of a single LCHC-actuator unit as well as data related to the solar altitude and azimuth angles,[38] we then realized prototype device designs that utilized multiple LCHC-actuator units for full-range artificial heliotropism. First, a typical range of solar altitude angle during a day at most locations in the U.S. (we took the U.S. as an example) is 0° (dawn or dusk) to 70° (midday). Second, though the solar azimuth angle range during a day at most U.S. locations varies, a coverage from 90° (6–8 am) to 270° (5–7 pm) in the azimuth angle would be sufficient. Therefore, a design utilizing three or four LCHC-actuator units (three shown in **Figure 6**) could provide full range of artificial heliotropism. The LCHC-actuator units were arranged centrosymmetrically, with a 60° angular separation between their medial axes. With this arrangement, 3 LCHC-actuator units were placed corresponding to azimuth angles of 120°, 180°, and 240°, respectively, and the resultant range of artificial heliotropism is essentially the superposition of that from each single unit. The increase in the solar cell photocurrent output with this device with 3 LCHC-actuator units vs. the direction of the incident light from the same white light source as above is shown in Figure 6a. As expected, at 0° altitude and 120°, 180°, or 240° azimuth, the heliotropic effect was the strongest, with an increase in the photocurrent by up to 3700%. The effective azimuth heliotropic range was indeed nearly tripled. The increase in photocurrent was more than 100% at 0° altitude. Within most of the 90° to 270° azimuth range, even when the altitude angle increased to 60°, the photocurrent was still increased by around 10%. Figure 6b,c show the images of this device in one

Adv. Funct. Mater. **2012**,
DOI: 10.1002/adfm.201202038

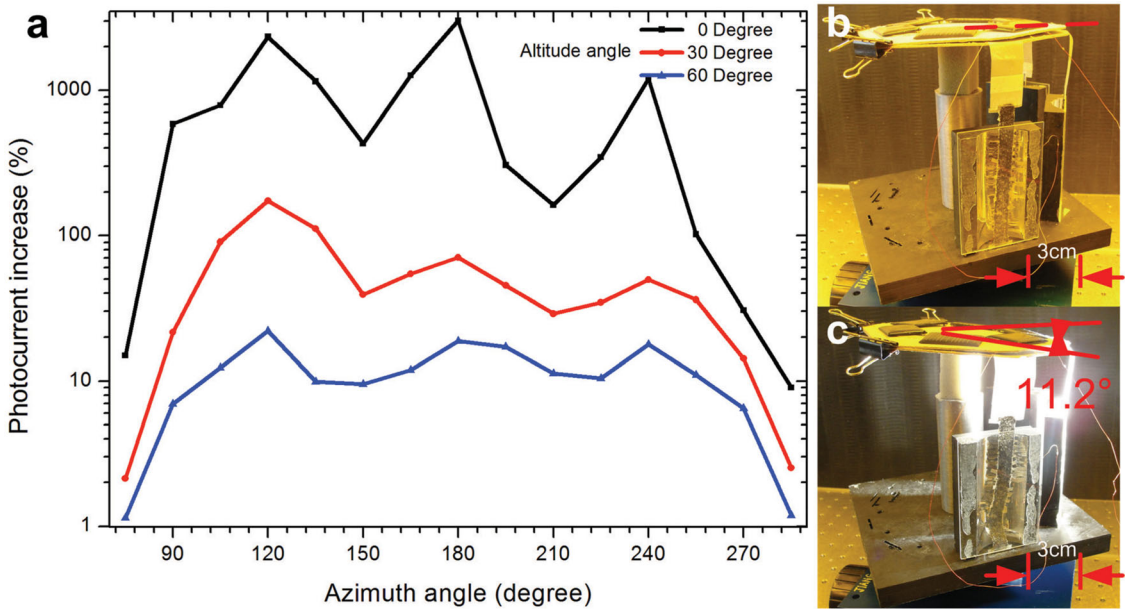

Figure 6. Photocurrent increase owing to artificial heliotropism by the prototype device with 3 LCHC-actuator units (a) and its heliotropic behavior in laboratory (b,c). An altitude-azimuth coordinate system similar to Figure 4d was used for data acquisition for (a). The origin was the center of the actuator in the middle. Irradiation was from a white light source (intensity: 100 mW cm^{-2}; partially collimated; spot diameter: 101.6 mm; 0° altitude; 180° azimuth) for (b,c). b) Before irradiation. c) 30 s after irradiation was on.

laboratory test; the platform with solar cells tilted towards the light source after the actuation (incident light: 0° altitude, 180° azimuth). In-field tests of a similar device with 4 LCHC-actuator units were conducted from August to September 2011 in Madison, WI, USA. Both the heliotropic range and the increase in the solar cell photocurrent output were consistent with the results obtained in the laboratory environment. More detail is included in the Supporting Information (Movies 4–6).

3. Conclusions

We have demonstrated artificial heliotropism for solar cells, utilizing fiber-network/SWCNT/LCE actuators that can be directly driven by the sunlight instead of relying on other power consuming components for tracking the sun and actuation. When these actuators face the sun, they contract, and as a result, tilt the solar cells towards the sun, thus the artificial heliotropism. Both laboratory tests and in-field tests confirmed that the devices were capable of full-range artificial heliotropism, with 60° of range in altitude angle, and 180° of range in azimuth angle. Significant increase in the output photocurrent of the solar cells was observed owing to the artificial heliotropism. In the future, we will improve the LCE nanocomposite for larger contraction ratio, lower threshold of response to the sunlight, and higher loading capability. We will investigate on improving the LCE matrix materials and the continuous fibers, as well as the effect of the orientations of carbon nanotubes in regard to the nematic LCE matrices on the nematic orders and the photo-thermomechanical actuation performance. We will also improve the design for more effective heliotropism, and scale up the system design to accommodate large solar panels. Our artificial heliotropism for solar energy harvesting is an effective approach to making the best use of the solar energy as a renewable clean energy source. Our approach can further be combined with others that aim to enhance the solar-to-electric conversion efficiency of the solar cells themselves and those that incorporate solar concentrators.

4. Experimental Section

Materials Preparation: The pendant mesogenic group, 4-methoxyphenyl-4-(1-buteneoxy) benzoate, and di-functional crosslinking group, 1,4 alkeneoxybenzene, were synthesized as reported previously.[33] The polymer backbone was a poly-methylhydrosiloxane (PMHS) with approximately 60 Si–H units per chain, obtained from ACROS Chemicals (Geel, Belgium). The commercial platinum catalyst dichloro(1,5-cyclooctadiene) platinum(II) was obtained from Sigma-Aldrich (St Louis, MO, USA). The catalyst solution was prepared by dissolving 0.025g of the dichloro(1,5-cyclooctadiene) platinum(II) in 2 mL of dichloromethane, then adding 20 mL of toluene.

The polyurethane fiber-network was obtained through slicing a polyurethane porous rubber to a lamella with the thickness of 0.4 mm. It became a flexible layer of polyurethane fiber-network with irregular meshes.

The synthesis of the side-chain nematic LCE networks with polysiloxane backbone, aligned in uniaxial orientation, was performed through a two-stage crosslinking coupled with a drawing process. The fabrication process of the fiber-network/SWCNT/LCE composite films with SWCNT/nematic LCE (the content of SWCNTs in LCE was about 0.45 wt%) as the matrix and polyurethane fiber-network as the reinforcement phase is shown in Figure 1. 4.2 mg of SWCNTs were mixed into the reaction mixture solution, which was 0.16 g of PMHS, 0.65 g of 4-methoxyphenyl-4-(1-buteneoxy) benzoate (2.18 mmol) and 0.088 g of 1, 4 alkeneoxybenzene (0.214 mmol) solved in 2.6 mL of toluene, under ultrasonication for better dispersion; the ultrasonic mixing was performed for about 2 min. 120 µL of catalyst solution was

added into the reaction mixture solution containing SWCNTs; then the solution was cast into a polytetrafluoroethylene (PTFE) rectangular parallel-piped mold with dimensions of 90 mm × 14 mm × 10 mm, on the bottom of which a rectangular lamella of polyurethane fiber-network with the length and width of 90 mm and 12 mm, respectively, was pre-laid. The precursors inside the mold was first ultrasonicated for 2.5 min to degas the mixture, then heated in an oven at 65 °C for 50 min for partial crosslinking process (first crosslinking stage). A swollen gel of partially crosslinked elastomer with the toluene solvent absorbed inside it was generated during this first crosslinking stage. Thereafter the mold was cooled to the room temperature. 7 mL of hexane was poured into the mold to facilitate the removal process of the partially crosslinked elastomer embedded with the polyurethane fiber-network, which was then carefully removed from the mold. The elastomer was immediately hung at one end with a clamp for drying at the room temperature. As the toluene contained in the partially crosslinked elastomer evaporated, the elastomer gradually shrank and the flexible polyurethane fiber-network shrank together. The drying process proceeded for about 40 min, and the composite film contracted to a stable length of about 6.3 cm from its original length of 9 cm. Subsequently the drawing process started, with the other free end of the composite film now loaded with a 6.5 g weight. The loading weight was increased step by step, with 2.5 g of increment every 2 h, to 14 g. After 12 h of gradual uniaxial stretch along the length by the load, the composite film extended to a stable length of about 9 cm and a nematic alignment in LCE matrix was obtained, while the embedded polyurethane fiber-network recovered to its initial length as the length of the composite film was stretched to be equal to that of the mold. Finally the composite film with the load was annealed at 70 °C overnight to complete the crosslinking reaction in the nematic phase (second crosslinking stage). All the prepared fiber-network/SWCNT/LCE composite films have dimensions around 90 mm × 12 mm × 0.8 mm.

Materials Characteristics and Methods: The photoactuation measurements of the LCE nanocomposites were performed by using a white light source (New Port, Oriel Productline, Model 66885, Irvine, CA). The phase transformation behaviors of the materials were investigated by differential scanning calorimetry (DSC) measurements (TA Instruments Q100 modulated differential scanning calorimeter, New Castle, DE, USA) at a heating and cooling rate of 10 K min^{-1}. X-ray diffraction spectra were measured by a Bruker/Siemens Hi-Star 2d X-ray Diffractometer with a monochromatic CuKalpha point source (0.8 mm). The materials' mechanical properties were measured with stress meters.

Light Concentrator/Heat Collectors (LCHCs): Bulk material (black PTFE), high-reflectivity multilayer polymer film, and high-transmittance glass were obtained from McMaster-Carr, Inc (Elmhurst, IL, USA). Bulk materials were processed by a conventional machining method using a mill (GEVS500A, Eisen Machinery, Inc., Santa Fe Springs, CA, USA). The polymer film was bonded on the PTFE bulk with double-sided adhesive tapes (3M Inc., St Paul, MN, USA).

Artificial Heliotropic Devices: Pedestals of the artificial heliotropic devices were also made from black PTFE, and were machined using a mill. Solar cells were fixed on a light-weight platform, and electrically connected in series. The commercial solar cells are rectangular in shape (length: 34 mm, width: 23 mm, from Hobby Engineering, Inc. (South San Francisco, CA, USA)). The platform was supported by an elastic beam, effectively reducing the driving force needed for the platform to tilt and ensuring the platform to restore to its initial (horizontal) state when the stimulating source (sunlight or light source) was removed.

In-Field Experiments: Artificial heliotropic devices with different configurations were tested under natural sunlight between July and September 2011, in Madison, WI. The Global Positioning System coordinates of the two testing locations in Madison, WI, USA were 43° 4′20″N and 89° 24′ 44″W (location I), and 43° 5′12″N and 89° 26′ 31″W (location II), respectively. Devices were fixed on rotational stages so that the directions that they faced could be adjusted. More detail is provided in the Supporting Information (Table S1 and Figure S9a,S10).

Experiments in the Laboratory: A white light source (New Port, Oriel Productline, Model 66885, Irvine, CA, USA) was used. The light beam from the light source was reflected by a mirror (diameter: 4 inch), whose position and reflection angle was varied to adjust the altitude angle of the incident light onto the solar cells. The intensity of the incident beam spot was kept at 100 mW cm^{-2}. The photocurrent output of the solar cells connected in series was monitored by a digital multimeter (Model 34401A, Agilent, Santa Clara, CA, USA). More detail is provided in the Supporting Information (Figure S9b).

Supporting Information

Supporting Information is available from the Wiley Online Library or from the author.

Acknowledgements

C.S.L. and Y.L. contributed equally to this work. This work was mainly supported by Wisconsin Institutes for Discovery and partly supported by the U. S. National Science Foundation under Grant ECCS 0702095. The authors thank N. L. Abbott, Z. Q. Yang, C.-W. Lo, B. Aldalali, P. Gopalan, G. Venkataramanan, and G. Lin for discussion.

Received: June 12, 2012
Revised: July 15, 2012
Published online:

[1] R. A. Sherry, C. Galen, *Plant Cell Environ.* **1998**, *21*, 983.
[2] C.-Y. Li, P.-C. Chou, C.-M. Chiang, C.-F. Lin, *Sensors* **2009**, *9*, 3875.
[3] H. Mousazadeh, A. Keyhani, A. Javadi, H. Mobli, K. Abrinia, A. Sharifi, *Renew. Sust. Energ. Rev.* **2009**, *13*, 1800.
[4] J. Weickert, R. B. Dunbar, H. C. Hesse, W. Wiedemann, L. Schmidt-Mende, *Adv. Mater.* **2011**, *23*, 1810.
[5] C. J. Brabec, S. Gowrisanker, J. J. M. Halls, D. Laird, S. J. Jia, S. P. Williams, *Adv. Mater.* **2010**, *22*, 3839.
[6] L. Chen, Z. Hong, G. Li, Y. Yang, *Adv. Mater.* **2009**, *31*, 1434.
[7] H. B. Yildiz, R. Tel-Vered, I. Willner, *Adv. Funct. Mater.* **2008**, *18*, 3497.
[8] J. F. Qian, P. Liu, Y. Xiao, Y. Jiang, Y. L. Cao, X. P. Ai, H. X. Yang, *Adv. Mater.* **2009**, *21*, 3663.
[9] H. J. Snaith, *Adv. Funct. Mater.* **2010**, *20*, 13.
[10] Y. H. Yu, P. V. Kamat, M. Kuno, *Adv. Funct. Mater.* **2010**, *20*, 1464.
[11] J. Krantz, M. Richter, S. Spallek, E. Spiecker, C. J. Brabec, *Adv. Funct. Mater.* **2011**, *21*, 4784.
[12] D. Kraemer, B. Poudel, H.-P. Feng, J. C. Caylor, B. Yu, X. Yan, Y. Ma, X. Wang, D. Wang, A. Muto, K. McEnaney, M. Chiesa, Z. Ren, G. Chen, *Nat. Mater.* **2011**, *10*, 532.
[13] J. Yoon, L. Li, A. V. Semichaevsky, J. H. Ryu, H. T. Johnson, R. G. Nuzzo, J. A. Rogers, *Nat. Commun.* **2011**, *2*, 343.
[14] M. J. Currie, J. K. Mapel, T. D. Heidel, S. Goffri, M. A. Baldo, *Science* **2008**, *321*, 226.
[15] M. R. Lee, R. D. Eckert, K. Forberich, G. Dennler, C. J. Brabec, R.. Gaudiana, *Science* **2009**, *324*, 232.
[16] J. W. Schwede, I. Bargatin, D. C. Riley, B. E. Hardin, S. J. Rosenthal, Y. Sun, F. Schmitt, P. Pianetta, R. T. Howe, Z. X. Shen, N. A. Melosh, *Nat. Mater.* **2010**, *9*, 762.
[17] F. Ercole, T. P. Davis, R. A. Evans, *Polym. Chem.* **2010**, *1*, 37.
[18] M. Warner, E. M. Terentjev, *Liquid Crystal Elastomers*, Oxford University Press, Oxford **2003**.
[19] A. Greve, H. Finkelmann, *Macromol. Chem. Phys.* **2001**, *202*, 2926.
[20] A. Kaiser, M. Winkler, S. Krause, H. Finkelmann, A. M. Schmidt, *J. Mater. Chem.* **2009**, *19*, 538.

[21] M. Chambers, H. Finkelmann, M. Remskar, A. Sanchez-Ferrer, B. Zalar, S. Zumer, *J. Mater. Chem.* **2009**, *19*, 1524.
[22] L. Q. Yang, K. Setyowati, A. Li, S. Q. Gong, J. Chen, *Adv. Mater.* **2008**, *20*, 2271.
[23] Y. Yu, M. Nakano, T. Ikeda, *Nature* **2003**, *425*, 145.
[24] M. Camacho-Lopez, H. Finkelmann, P. Palffy-Muhoray, M. Shelley, *Nat. Mater.* **2004**, *3*, 307.
[25] A. Buguin, M. H. Li, P. Silberzan, B. Ladoux, P. Keller, *J. Am. Chem. Soc.* **2006**, *128*, 1088.
[26] M. Yamada, M. Kondo, J. I. Mamiya, Y. L. Yu, M. Kinoshita, C. J. Barrett, T. Ikeda, *Angew. Chem. Int. Ed.* **2008**, *47*, 4986.
[27] M. Yamada, M. Kondo, R. Miyasato, Y. Naka, J. Mamiya, M. Kinoshita, A. Shishido, Y. L. Yu, C. J. Barrett, T. Ikeda, *J. Mater. Chem.* **2009**, *19*, 60.
[28] C. L. Van Oosten, C. W. M. Bastiaansen, D. J. Broer, *Nat. Mater.* **2009**, *8*, 677.
[29] F. Cheng, R. Yin, Y. Zhang, C.-C. Yen, Y. Yu, *Soft. Matter* **2010**, *6*, 3447.
[30] S. Serak, N. Tabiryan, R. Vergara, T. J. White, R. A. Vaia, T. J. Bunning, *Soft. Matter* **2010**, *6*, 779.
[31] A. Sanchez-Ferrer, T. Fischl, M. Stubenrauch, A. Albrecht, H. Wurmus, M. Hoffmann, H. Finkelmann, *Adv. Mater.* **2011**, *23*, 4526.
[32] P. M. Ajayan, M. Terrones, A. de la Guardia, V. Huc, N. Grobert, B. Wei, H. Lezec, G. Ramanath, T. W. Ebbesen, *Science* **2002**, *296*, 705.
[33] C. Li, Y. Liu, C.-W. Lo, H. Jiang, *Soft. Matter* **2011**, *16*, 7511.
[34] W. Wang, X. Sun, W. Wu, H. Peng, Y. Yu, *Angew. Chem. Int. Ed.* **2012**, *51*, 4644.
[35] J. Cviklinski, A. R. Tajbakhsh, E. M. Terentjev, *Eur. Phys. J. E.* **2002**, *9*, 427.
[36] S. Courty, J. Mine, A. R. Tajbakhsh, E. M. Terentjev, *Europhys. Lett.* **2003**, *64*, 654.
[37] M. J. Robert, *Mechanics of Composite Materials*, McGraw-Hill Book Company, New York **1975**.
[38] The U.S. Naval Observatory (USNO), *Sun or Moon Altitude/Azimuth Table*, http://aa.usno.navy.mil/data/docs/RS_OneDay.php (accessed February 2012).